Proc. 5th Int. Symp. Turbulence and Shear Flow Phenomena
Munich, Germany, August 27-29, 2007, pp. 727-732.

OPTIMIZATION OF AN ANISOTROPIC COMPLIANT SURFACE FOR TURBULENT FRICTION DRAG REDUCTION

Koji Fukagata
Department of Mechanical Engineering
Keio University
Hiyoshi 3-14-1, Kohoku-ku, Yokohama 223-8522, Japan
fukagata@mech.keio.ac.jp

Stefan Kern, Philippe Chatelain, Petros Koumoutsakos
Computational Science and Engineering Laboratory
ETH Zürich
CH-8092, Switzerland
skern@inf.ethz.ch, pchatela@inf.ethz.ch, petros@ethz.ch

Nobuhide Kasagi
Department of Mechanical Engineering
The University of Tokyo
Hongo 7-3-1, Bunkyo-ku, Tokyo 113-8656, Japan
kasagi@thtlab.t.u-tokyo.ac.jp

ABSTRACT

The direct numerical simulation (DNS) of the channel flow with an anisotropic compliant surface is performed in order to investigate its drag reduction effect in a fully developed turbulent flow. The surface is passively driven by the pressure and wall-shear stress fluctuations, and the surface velocity provides a boundary condition for the fluid velocity field. A stochastic optimization method (CMA-ES) is used to optimize the parameters of the anisotropic compliant surface. The optimization identifies several sets of parameters that result in a reduction of the friction drag with a maximum reduction rate of 8%. The primary mechanism for drag reduction is attributed to the decrease of the Reynolds Shear Stress (RSS) near the wall induced by the anisotropic structure and kinematics of the surface. The resultant wall motion is a uniform wave traveling downstream.

INTRODUCTION

Compliant surfaces have attracted considerable attention as potential passive mechanisms to reduce turbulent friction drag. For laminar-turbulence transition, several theoretical and experimental studies have been reported (see Gad-el-Hak (2002) and references therein), and it is now believed that such surfaces can delay transition. For fully-developed wall-bounded turbulent flow, however, drag reduction effect by compliant surfaces has been in question for a long time.

Recently, several Direct Numerical Simulation (DNS) studies have tried to clarify whether or not the friction drag is reduced by compliant surfaces and the mechanism of drag reduction. Endo and Himeno (2002) performed DNS of turbulent channel flow with a simplified isotropic compliant surface as shown in Fig. 1b, which models Kramer's coating (Fig. 1a), and reported a 2.7% drag reduction. This result was soon disproved by a similar DNS by Xu et al. (2003), in which no clear drag reduction effect was obtained. The major difference between Endo and Himeno (2002) and Xu et al. (2003) is the integration time for the statistics accumulation; $t^{+0} = 0-1000$ in the former and $t^{+0} = 500-3000$ in the latter (where the superscript "+0" denotes the wall unit in the case of solid channel). Xu et al. (2003) concluded that the drag reduction observed by Endo and Himeno (2002) was merely a transitional one. More importantly, their analysis clearly shows that the pressure fluctuation and the wall deformation cannot be in-phase, although these should become in-phase in order to reduce the drag. This analysis implies that one may need a driving force other than pressure in order to have a surface motion that reduces the friction drag.

In the present study, we perform DNS of channel flow with a compliant surface. In contrast to the previous DNS studies, we consider an anisotropic compliant surface (Carpenter and Morris, 1990), as shown in Fig. 1d, which models Grosskreutz's compliant wall (Fig. 1c). This anisotropic surface has, at least, two differences when compared to the isotropic one:

1. The surface is driven also by the wall-shear, which can become in-phase with the induced wall velocity;

2. Due to the constraint of the inclined arms, the wall moves so as to weaken the RSS, $-\overline{u'v'}$ (Fig. 2).

The latter difference is directly related to the reduction of friction drag because of the identity between the RSS and the skin friction coefficient, C_f (Fukagata et al., 2002; Bewley and Aamo, 2004), i.e.,

$$C_f = \frac{12}{Re_b} + 24 \int_0^1 (1-y)\,(-\overline{u'v'})\,dy \qquad (1)$$

(this is the identity equation for channel flows and all the variables are made dimensionless by using the channel half width and twice the bulk mean velocity.)

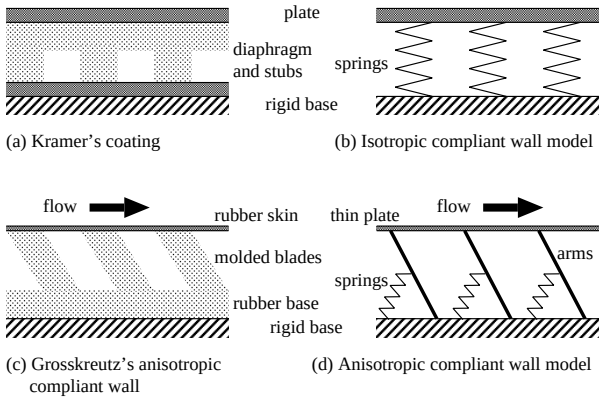

Figure 1: Schematics of compliant walls and their models (Redrawn based on Gad-el-Hak (2002)).

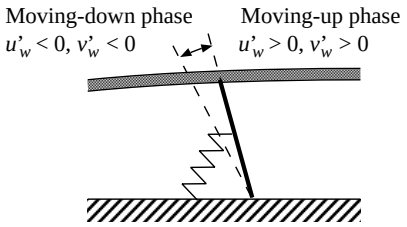

Figure 2: Restricted movement of anisotropic compliant wall that makes negative Reynolds shear stress on the wall.

ANISOTROPIC COMPLIANT WALL MODEL

Equation of motion

The movement of the arm is restricted in the streamwise (x)−wall-normal (y) plane (Fig. 3). Assuming a small change of arm angle, $\delta\theta$, from the equilibrium angle, θ, the governing equation for the surface can be written for a single variable, $\eta_f(x, z, t)$, as

$$\eta_f = l\delta\theta \ , \tag{2}$$

where l is the arm length. The displacement (x'_w, y'_w, z'_w) and the velocity (u'_w, v'_w, w'_w) of the membrane are given by

$$x'_w = \eta_f \sin\theta \ , \quad y'_w = \eta_f \cos\theta \ , \quad z'_w = 0 \ , \tag{3}$$

and

$$u'_w = \frac{\partial \eta_f}{\partial t}\sin\theta \ , \quad v'_w = \frac{\partial \eta_f}{\partial t}\cos\theta \ , \quad w'_w = 0 \ , \tag{4}$$

respectively.

The governing equation of motion for η_f has been modified from the original one (Carpenter and Morris, 1990) so as to allow two-dimensional deformation. Expressed in wall units, this equation reads

$$\begin{aligned} b^+\rho_m^+\frac{\partial^2\eta_f^+}{\partial t^{+2}} + D^+\frac{\partial^+\eta_f^+}{\partial t^+} + B^+\cos^2\theta\nabla^{+4}\eta_f^+ \\ -E^+b^+\sin^2\theta\nabla^{+2}\eta_f^+ + K_E^+\eta_f^+ = f^+ \ , \end{aligned} \tag{5}$$

where

$$f^+ = (-p'^+_w + \sigma'^+_w)\cos\theta + \tau'^+_w\sin\theta \tag{6}$$

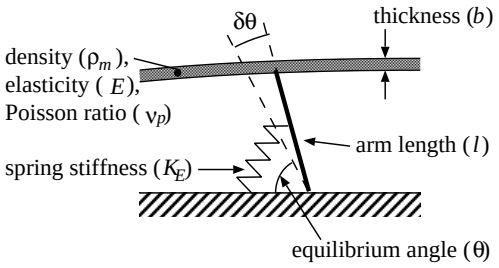

Figure 3: Parameters of the anisotropic compliant wall model.

and $\nabla^2 = \partial^2/\partial x^2 + \partial^2/\partial z^2$. The wall units variants of the membrane parameters are defined by

$$\begin{cases} \rho_m^+ = \dfrac{\rho_m}{\rho} \ , & b^+ = \dfrac{bu_\tau}{\nu} & D^+ = \dfrac{D}{\rho u_\tau} \ , \\ E^+ = \dfrac{E}{\rho u_\tau^2} \ , & K_E^+ = \dfrac{K_E\nu}{\rho u_\tau^3} \ . \end{cases} \tag{7}$$

where b, ρ_m and E are, respectively, the thickness, the density, the elastic modulus of the membrane, K_E is the spring stiffness. The flexural rigidity of the membrane, B, in this case is given by

$$B = \frac{Eb^3}{12(1-\nu_p^2)} \ , \tag{8}$$

where ν_p is the Poisson ratio. A damper designed by the parameter D is added to the spring. The driving forces are fluctuations of the pressure p'_w, the normal stress, σ'_w, and the shear stress, τ'_w.

Monoharmonic analysis

Two-dimensional Fourier transform of the membrane equation of motion results in the equation of motion for the standard spring-mass-damper system, i.e.,

$$\frac{\partial^2\hat{\eta_f}}{\partial t^2} + 2\zeta\omega_n\frac{\partial\hat{\eta_f}}{\partial t} + \omega_n^2\hat{\eta}_f = \frac{\hat{f}}{b\rho_m} \ , \tag{9}$$

where

$$\omega_n = \sqrt{\frac{K_E + Bk^4\cos^2\theta + Ebk^2\sin^2\theta}{b\rho_m}} \tag{10}$$

is the natural angular frequency of the wavenumber mode k (with $k = \sqrt{k_x^2 + k_z^2}$) and

$$\zeta = \frac{D}{2b\rho_m\omega_n} \tag{11}$$

is the damping coefficient. From the classical control theory, the gain and phase delay for the velocity can be found as

$$|\hat{G}(i\omega)| = \frac{\left(\dfrac{\omega}{\omega_n}\right)}{b\rho_m\sqrt{\left[1-\left(\dfrac{\omega}{\omega_n}\right)^2\right]^2 + \left(2\zeta\dfrac{\omega}{\omega_n}\right)^2}} \tag{12}$$

and

$$\angle\hat{G}(i\omega) = \tan^{-1}\left[\frac{1-\left(\dfrac{\omega}{\omega_n}\right)^2}{2\zeta\dfrac{\omega}{\omega_n}}\right] \ , \tag{13}$$

respectively. The form of these equations is exactly the same as that of the isotropic compliant surface (Xu et al., 2003). We note however that the relationship between the oscillation frequency and the wavenumber (Eq. (10)) and the composition of the driving force (Eq. (6)) are different.

NUMERICAL PROCEDURE

Direct numerical simulation

We consider an incompressible turbulent channel flow. The fluid velocity field is simulated by using the finite difference code, which was originally developed for pipe flows (Fukagata and Kasagi, 2002) and later modified to channel flows (Fukagata et al., 2006). The flow rate is kept constant. The bulk Reynolds number, Re_b, is 3300, which corresponds to a friction Reynolds number of about 110 ($Re_\tau = 112.46$) in the case of rigid walls. The computational domain is $3\delta \times 2\delta \times 3\delta$ and the number of cells is $32 \times 64 \times 64$ in the streamwise (x), the wall-normal (y), and the spanwise (z) directions, respectively. This domain size is similar to that used in the previous study of isotropic compliant surfaces by Xu et al. (2003).

The membrane equation of motion (5) is spatially discretized by the second-order accurate finite difference method and temporally integrated by the third order low storage Runge-Kutta/Crank Nicolson (RK3/CN) method. The membrane is driven by the pressure and wall-shear fluctuations as described by Eq. (5), whereas the velocity of the membrane computed at every instant is fed back to the fluid velocity field as the boundary condition at the wall, i.e., Eq. (4). In order to enable an optimization study, deformation of the membrane is neglected.

The computational time step is chosen so that both the CFL number for the fluid and that for the membrane (determined by the wavespeed) are less than 0.5. The wavespeed of the membrane in the case without force and damping is (Carpenter and Morris, 1990)

$$c = \frac{\omega_n}{k} \ . \tag{14}$$

The computation is started from the velocity field of a solid channel flow and integrated for $t^{+0} = 0 - 12000$. The statistics presented below are accumulated during the time period of $t^{+0} = 6000 - 12000$, which is twice as long as that used by Xu et al. (2003).

Stochastic optimization

The monoharmonic analysis of the compliant wall model gives us an estimate of the wavelike behavior of the wall, but cannot predict the highly nonlinear interaction of the wall with the turbulent flow. In order to systematically investigate the capabilities of the proposed compliant surface design, an inverse design procedure is used to find optimal parameters for the model.

The inverse design problem is formulated as an optimization problem, where we try to minimize the drag coefficient C_f of the turbulent channel flow as a function of the wall parameters b, ρ_m, E, K_E, θ, and D. As we assume small deformations of the compliant wall in the computation, we require $\eta^{+0}_{f,rms} < 5$. Combined into one expression the loss function L to be minimized reads

$$L(\boldsymbol{\alpha}) = C_f(\boldsymbol{\alpha}) + c_\eta H\left(\eta^{+0}_{f,rms}(\boldsymbol{\alpha}) - 5\right) \cdot \left(\eta^{+0}_{f,rms}(\boldsymbol{\alpha}) - 5\right)^2 , \tag{15}$$

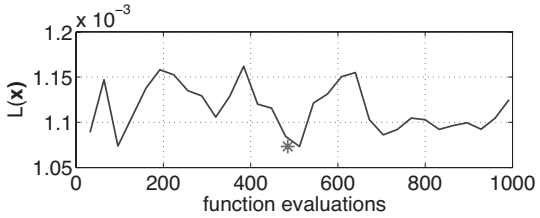

Figure 4: History of loss function, $L(\boldsymbol{\alpha})$, of the best individual in every generation. The star symbol denotes the loss function value of best parameter set found in the present optimization attempt.

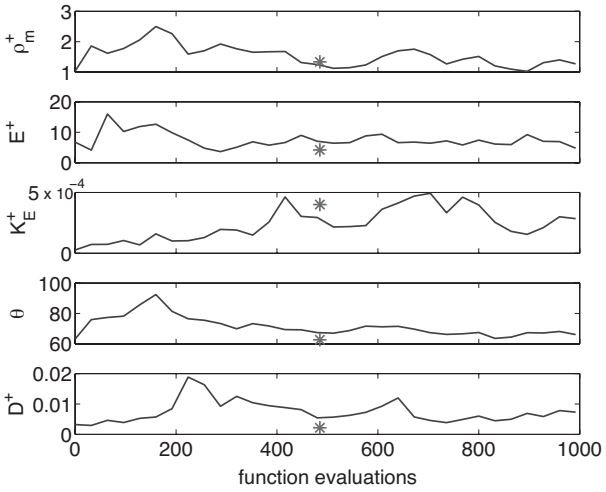

Figure 5: History of the population mean of parameters of the compliant wall. The star symbol denotes the best parameter set found in the present optimization attempt.

where $\boldsymbol{\alpha}$ are the encoded model parameters, c_η is a constant scaling factor for the penalty term, and $H(.)$ is the Heaviside function.

The turbulent channel flow coupled with the compliant walls is a highly dynamical system that is susceptible to small changes in design parameters requiring a optimization algorithm that is robust in the presence of uncertainties and possibly multiple optima. In addition, the algorithm should be highly efficient since the evaluation of $L(\boldsymbol{\alpha})$ using DNS is computationally intensive even with the velocity coupling only. We implement an *Evolution Strategy with Adaptation of the Covariance Matrix* (CMA-ES) (Hansen and Ostermeier, 2001, Hansen et al., 2003, Hansen and Kern, 2004). The competitive performance and robustness of CMA-ES have been demonstrated in a number of benchmark optimization problems (Kern et al., 2004) and applications. Based on a preliminary parameter study we choose a logarithmic encoding for all parameters except θ; the thickness b^{+0} is kept constant:

$$\begin{array}{rcll} \rho_m^{+0} & = & 1.0 \times 10^{\alpha_1}, & \alpha_1 \in [-1, 1], \\ b^{+0} & \equiv & 1.1, & \\ E^{+0} & = & 6.3 \times 10^{\alpha_2}, & \alpha_2 \in [-1, 1], \\ K_E^{+0} & = & 8.2 \times 10^{\alpha_3}, & \alpha_3 \in [-5, 2], \\ \theta & = & 30 \times \alpha_4 \text{ deg.}, & \alpha_4 \in [1, 3], \\ D^{+0} & = & 3.0 \times 10^{\alpha_5}, & \alpha_5 \in [-3, -1]. \end{array} \tag{16}$$

The population size is set to $\lambda = 32$ which is 4 times the

default population size for problem dimension 5 (Hansen et al., 2003). An increased population size for CMA-ES generally improves the robustness of the algorithm against noise and multimodality; it also reduces the number of generations needed to reach a given convergence level. The evaluation of the populations is performed in parallel. The uncertainty in the evaluation of $C_f(\boldsymbol{\alpha})$ is reduced by actually performing two evaluations starting from different initial conditions. In addition, the twofold evaluation allows for a simple yet efficient load balancing by pairing cases with small and large time-steps on the individual CPUs.

RESULTS AND DISCUSSION

Optimization results

The CMA-ES was initialized with the best parameter set found in the preliminary parameter survey mentioned above. The available computation time permitted 1000 evaluations of the loss function, $L(\boldsymbol{\alpha})$, each one involving two simulations with different initial turbulent fields. As Figs. 4 and 5 imply, the results of the optimization procedure using CMA-ES are ambivalent: while some very promising solutions are found, the algorithm does not show clear signs of converging to a optimal solution within the given limit of function evaluations.

Table 1 summarizes three cases. A case consists of a parameter set and the resulting function value; each case is designated by its position in the sequence of the function evaluations (Fig. 4). The table shows the two best cases obtained in the present optimization attempt (Case 89 and Case 587) and a case of drag increase (Case 821). While not far from each other, the actual parameter figures for the two best cases confirm that the algorithm has not converged yet. This also hints at the multimodality of the underlying physics.

The table also shows the resultant drag reduction rate (R_D) and the computed root-mean-square (RMS) wall displacement (y^{+0}_{rms}). Drag reduction is attained in Cases 89 and 516, which amounts to $7-8\%$. The time trace of the normalized skin friction coefficient, as shown in Fig. 6, confirms the drag reduction in these two cases, too, although the fluctuation is relatively large due to the very low Reynolds number and the small computational domain used. An interesting observation in Table 1 is that the equilibrium arm angle (θ) of the best two cases is about $60°$, keeping in mind that the optimization is made in the range of $30° < \theta < 90°$. This angle makes the wall structure quite sensitive to the wall shear stress and suggests that this quantity drives motions that play an important role for drag reduction, as anticipated in our comparison with isotropic compliant wall.

Table 1: The parameters of two best cases (Case 89 and Case 587) and a case of drag increase (Case 821) (in wall units of solid channel) and the resultant drag reduction rate (R_D) and RMS wall displacement ($y^{+0}_{w,rms}$).

Case	**89**	**516**	**821**
ρ_m^{+0}	1.23×10^{0}	1.34×10^{0}	7.42×10^{-1}
E^{+0}	2.61×10^{0}	4.03×10^{0}	1.12×10^{0}
K_E^{+0}	3.25×10^{-4}	3.75×10^{-4}	8.62×10^{-5}
θ [deg.]	62.7	62.7	63.9
D^{+0}	6.49×10^{-4}	2.12×10^{-3}	1.29×10^{-3}
R_D [%]	8.32	7.00	−10.7
$y^{+0}_{w,rms}$	3.67	3.14	6.10

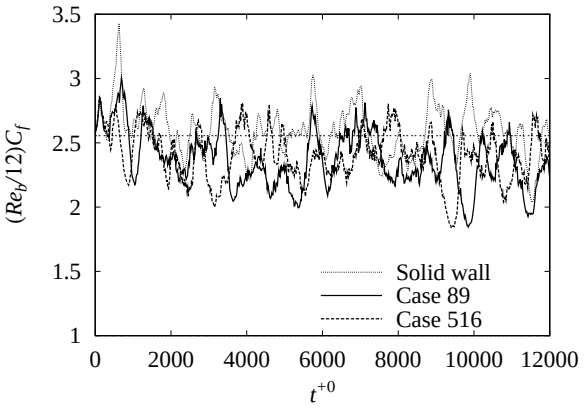

Figure 6: Time trace of the friction drag normalized by the laminar drag.

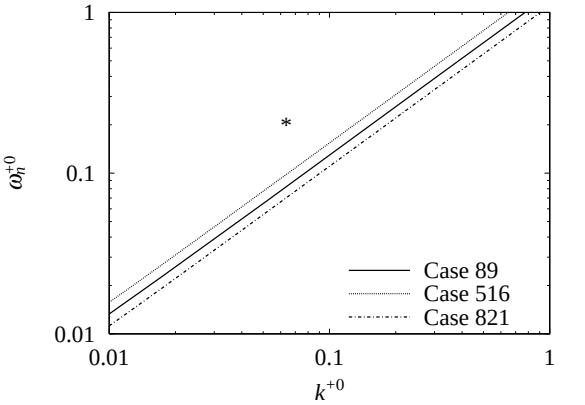

Figure 7: Oscillation frequency (ω_n) as a function of two-dimensional wavenumber (k). The asterisk at $(k^{+0}, \omega^{+0}) = (0.06, 0.2)$ corresponds to the typical scale of quasi-streamwise vortices.

Figure 7 shows the relationship between the two-dimensional wavenumber, k, and the oscillation frequency, ω_n (see, Eq. (10)), of the cases above. These surfaces have much lower oscillation frequency than the frequency of streamwise vortices. From this viewpoint, Case 821 (which results in drag increase) has similar characteristics to those of Cases 89 and 516. The major difference is that Case 821 has slightly softer membrane and spring, which results in a larger wall displacement, y^{+0}_{rms}.

Turbulence statistics

Figure 8 shows the Reynolds shear stress (RSS) of three cases in Table 1. In all cases, the RSS takes a negative value on the wall. This is actually enforced by the design of the surface: its motion is restricted by the inclined arm (Fig. 2). In accordance with the identity equation (1), the RSS is significantly reduced in Cases 89 and 516, except for the region of $2 < y^{+0} < 7$. In Case 821, in contrast, the RSS is slightly decreased far from the wall but significantly increased near the wall, which causes the drag increase.

The RMS velocity components are shown in Fig. 9. In the drag reducing case (Case 89), the wall-normal component (v_{rms}) is nearly unchanged, whilst the streamwise component (u_{rms}) is reduced near the wall. This reduction

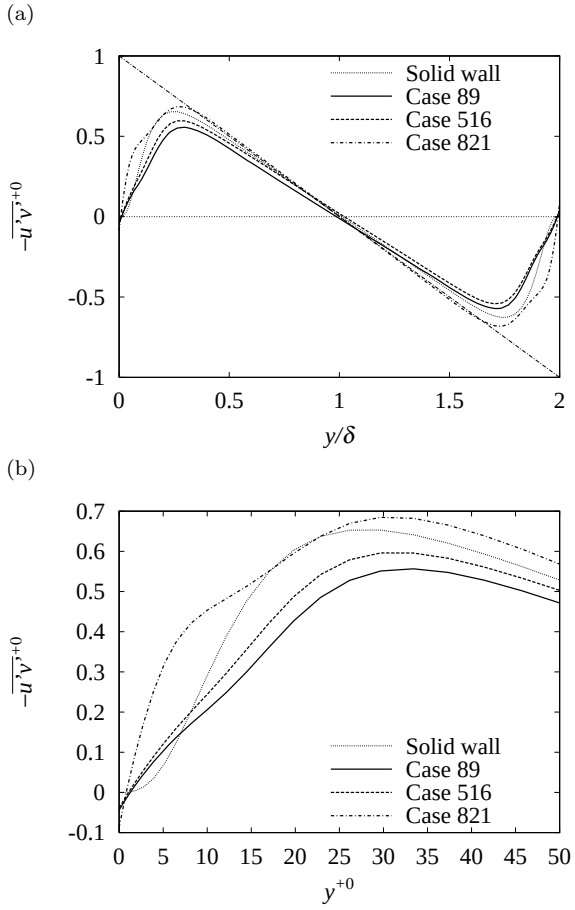

Figure 8: Reynolds shear stress: (a) overview; (b) near the wall.

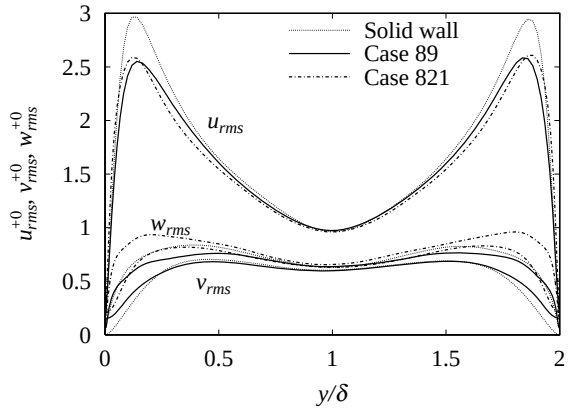

Figure 9: RMS velocity components.

of u_{rms} directly leads to the reduction of the RSS. Although u_{rms} is reduced also in the drag increasing case (Case 821), v_{rms} is also increased in this case. From this observation, the common effect of the present anisotropic compliant wall seems to be the reduction of the streamwise RMS velocity and the enhancement of the wall-normal RMS velocity. The reduction of the RSS (and the friction drag) seems to occur only when the v_{rms} induced by the wall-motion is not too large.

Motion of anisotropic compliant surface

Figure 10 shows the motion of two drag reducing cases (Cases 89 and 516). Both cases display a surface which deforms in a wavelike manner, traveling in the downstream direction. The wavelength is about 330 wall unit (i.e., the same length as the computational domain) and the wavespeed is $c^{+0} = 0.38$. In terms of the bulk velocity, this corresponds to $c/U_b = 0.026$.

In Koumoutsakos (1999), traveling waves of blowing and suction have been reported as the result of a feedback vorticity flux control leading to large drag reductions. Recently, Min et al. (2006) recovered the traveling-wave-like blowing and suction in DNS and demonstrated that this type of motion can generate a negative RSS near the wall and thus reduce the drag. We wish to emphasize at this point that our study recovers a similar motion with a passive device.

Our best points are somewhat in contradiction with those of Min et al. (2006). For blowing and suction control, the linear analysis of Min et al. (2006) shows that downstream going waves always lead to a drag increase. Our results indicate otherwise for a compliant surface. The difference originates from the existence of streamwise velocity component on the wall. While the negative RSS is caused by the phase difference between u' and v' in the case of Min et al. (2006), the RSS on the wall is always made negative by the present anisotropic surface, as was illustrated in Fig. 2 and as was verified in Fig. 8.

CONCLUSIONS

We performed DNS of turbulent channel flow at $Re_{\tau 0} \simeq 110$ with an anisotropic compliant surface. The CMA-ES was used to simultaneously optimize five parameters. Although the CMA-ES did not converge within a given computational time, we obtained several sets of parameters that lead to a reduction of the friction drag. The maximum drag reduction rate attained in the present optimization attempt was 8%.

Both in the drag reducing and drag increasing cases, the Reynolds Shear Stress on the wall was found to become negative due to the motion of surfaces restricted by the inclined arms. We also observed a very reduced streamwise RMS velocity component near the wall. The difference between the drag reducing and drag increasing cases is the wall-normal RMS velocity component: it is kept at a level comparable to the one in the solid channel in the drag reducing cases, while it is significantly increased in the drag increasing cases.

The equilibrium arm angle of the drag reducing cases was about 60°. It implies that the wall-shear stress is an important driving force for the surface motion. The resultant surface motion was found to be a traveling wave. Unlike the recent study by Min et al. (2006), our best points show that for a compliant surface, a downstream traveling pattern achieves drag reduction.

Finally, while promising, our results also invite some caution about their breadth. The base wavelength of our best surface motions occupies the whole computational domain. A more conclusive investigation will thus require the use of a longer domain. Additionally, this will enable the study of the correlations between the flow structures and the wall deformations. This is left as a direction for possible future work.

ACKNOWLEDGMENT

The authors wish to acknowledge support by the Univer-

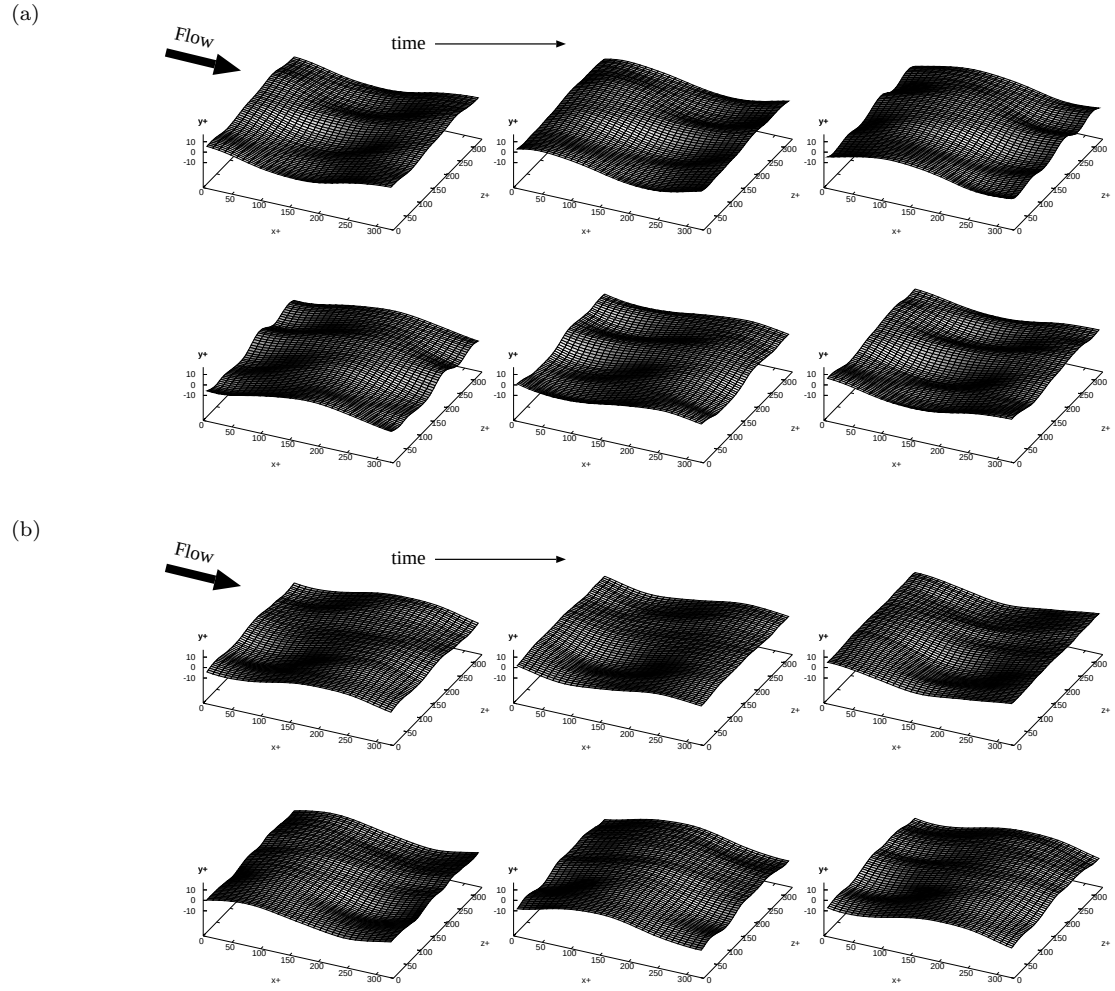

Figure 10: Surface motion: (a) Case 89; (b) Case 516.

sity of Tokyo – ETH Zürich exchange agreement.

REFERENCES

Bewley, T. R. and Aamo, O. M., "A "win-win" mechanism for low-drag transients in controlled 2D channel flow and its implications for sustained drag reduction," *J. Fluid Mech.* **499**, 183-196 (2004).

Carpenter, P. W. and Morris, P. J., "The effect of anisotropic wall compliance on boundary-layer stability and transition," *J. Fluid Mech.* **218**, 171-223 (1990).

Endo, T. and Himeno, R., "Direct numerical simulation of turbulent flow over a compliant surface," *J. Turbul.* **3**, 007 (2002).

Fukagata, K., Iwamoto, K., and Kasagi, N., "Contribution of Reynolds stress distribution to the skin friction in wall-bounded flows," *Phys. Fluids* **14**, L73-L76 (2002).

Fukagata, K. and Kasagi, N., "Highly energy-conservative finite difference method for the cylindrical coordinate system," *J. Comput. Phys.* **181**, 478-498 (2002).

Fukagata, K., Kasagi, N., and Koumoutsakos, P., "A theoretical prediction of friction drag reduction in turbulent flow by superhydrophobic surfaces," *Phys. Fluids* **18**, 051703 (2006).

Gad-el-Hak, M., "Compliant coatings for drag reduction," *Prog. Aerospace Sci.* **38**, 77-99 (2002).

Hansen, N., and Ostermeier, A., "Completely derandomized selfadaptation in evolution strategies," *Evol. Comput.* **9**, 159-195 (2001).

Hansen, N., Müller, S. D., and Koumoutsakos, P., "Reducing the time complexity of the derandomized evolution strategy with covariance matrix adaptation (CMA-ES)," *Evol. Comput.* **11**, 1-18 (2003).

Hansen, N. and Kern, S., "Evaluating the CMA evolution strategy on multimodal test functions," *Parallel Problem Solving from Nature - PPSN VIII*, 282-291 (2004).

Kern, S., Müller, S. D., Hansen, N., Büche, D., Ocenasek, J., Koumoutsakos, P., "Learning probability distributions in continuous evolutionary algorithms - a comparative review," *Natural Computing* **3**(1), 77-112 (2004).

Koumoutsakos, P., "Vorticity flux control in a turbulent channel flow," *Phys. Fluids* **11**, 248-250 (1999).

Min, T., Kang, S. M., Speyer, J. L., and Kim, J., "Sustained sub-laminar drag in a fully developed channel flow," *J. Fluid Mech.* **558**, 309-318 (2006).

Xu, S., Rempfer, D., and Lumley, J., "Turbulence over a compliant surface: numerical simulation and analysis," *J. Fluid Mech.* **478**, 11-34 (2003).